Hindawi
Mathematical Problems in Engineering
Volume 2020, Article ID 4651823, 12 pages
https://doi.org/10.1155/2020/4651823

Research Article

An Improved MPC-Based SVPWM Mechanism for NPC Three-Level Z-Source Converters

Wenbao Hou,[1,2,3] **Guojun Tan**,[1] **and Delu Li**[2]

[1]*School of Electrical and Power Engineering, China University of Mining and Technology, Xuzhou, China*
[2]*JiangSu Vocational Institute of Architectural Technology, Xuzhou, China*
[3]*JiangSu Collaborative Innovation Center for Building Energy Saving and Construction Technology, Xuzhou, China*

Correspondence should be addressed to Guojun Tan; gjtan_cumt@163.com

Received 14 April 2020; Accepted 22 June 2020; Published 12 August 2020

Guest Editor: Yi Qi

Model predictive control (MPC) method has been widely used to reduce the computational complexity of the traditional space vector pulse width modulation (SVPWM). However, for a neutral-point clamped three-level Z-source converter, the performance of the normal MPC strategy would highly depend on the computation processing rate because of the multiple times optimization calculation. In this paper, an improved MPC strategy has been developed, with a voltage prediction being designed to replace the current prediction, the calculation of the roll optimization could be effectively simplified significantly, and then the digital execution efficiency would be improved. Besides, in order to obtain a fixed output harmonic frequency, a combination of this improved MPC and SVPWM has been studied and the shoot-through state insertion for the Z-source also has been analyzed in detail. Lastly, comparison experiments have been carried out to make verification of this improved modulation mechanism.

1. Introduction

NPC three-level converters have significant advantages, e.g., smaller device pressure, lower dv/dt, and better harmonic distortion in the output [1, 2]. With a Z-source network, this NPC three-level converters would have a wide range of adjustable voltage, some allowed shoot-through states and better harmonic distortion in the output, and have been widely used in the photovoltaic(PV) grid-connecting system and the ac drive field [3–8]. For example, a switched quasi-Z-source DC-DC inverter has been used for PV Systems [9], and a novel Z-source three-level four-leg inverter has been researched to reduce the leakage current for three-phase PV inverters [10]. Nevertheless, the control difficulty, e.g., modulation method and stability assurance, would also increase because of the existing of Z-source network.

In terms of modulation, many improved algorithms have been proposed, e.g., in [6], the space vectors pulse width modulation along with the shoot-through insertions were introduced to the single Z-source NPC three-level inverters. A pulse width modulation (PWM) based on the stage-space averaging model was researched in [11] for a novel quasi-Z-source inverter topology. In [12], a new modulation strategy was studied in detail to reduce the leakage current for the Z-source four-leg inverters. In [13], a hybrid switching method with the combination of the PWM and pulse amplitude modulation (PAM) was proposed in details, which might result in a complicated computation and a high switching frequency and a switching loss reduction method based on a modified space vector modulation strategy [14].

In the past few years, the finite control set model predictive control (FCS-MPC) has been widely used in the modern power electrical areas for its fast response and being suitable for the multivariable and nonlinear systems [1, 15, 16]. In [17], the high performance MPC method has been used for the quasi-impedance source inverter and a FCS-MPC method was studied in [18]for the quasi-Z-source four-leg inverters with the consideration of an unbalanced load

condition. In [19, 20], model predictive control based on the discrete models were also presented. In [21], the MPC strategy with a ripple power compensation structure was presented for the Z-source converters, and the corresponding output harmonic distortions were random which were unsuitable for the filtering.

Unfortunately, when the MPC method was used for the NPC three-level converters, the control performance could be influenced because of the excessive optimization calculations, and for these NPC three-level converters, which combined with the Z-source network, how to make insertions for the shoot-through states is also one of the difficulties. In [22], a modified MPC method by using a novel voltage prediction has been studied for the grid-connected T-type inverter, which could improve the execution efficiency.

In order to solve the above problems and develop an efficient modulation approach for the NPC three-level ZSC to simplify the control complexity, an improved MPC-based SVPWM mechanism has been presented in this paper. In detail, a voltage prediction was designed instead of the normal current prediction, and the calculation of the roll optimization could be simplified significantly although the optimization times are the same. Besides, in order to obtain a relative fixed output harmonic frequency, the optimized voltage vector resulted from the improved MPC method then was generated by the basic vectors of the normal SVPWM and the insertions of the shoot-through states also have been studied in detail.

This study is organized into five sections. Following the introduction, the operation principle of the NPC three-level ZSC is explained in Section 2. In Section 3, this improved MPC-based SVPWM mechanism has been introduced in detail with the comparison to the traditional MPC method. Section 4 illustrates the experimental results with the performance comparisons between the traditional SVPWM strategy. Finally, some conclusions are drawn in Section 5.

2. Operation Principle of the NPC Three-Level Z-Source Converters

The NPC three-level ZSC researched in this paper is shown in Figure 1, containing two independent DC-power supplies. The connection point O of supplies is also regarded as the zero potential linking with the clamped point.

If the three up switches turn on (e.g., SA_1, SA_2, and SA_3), it is called upper shoot-through (UST) status being denoted as status "U." On the contrary, if the three down switches turn on, it is called down shoot-through status (DST), which is represented as status "D." The different states of this topology is summarized in Table 1.

Hypothesis $C_1 = C_2$ and $L_1 = L_2$ (means $V_{C1} = V_{C2} = V_C$ and $V_{L1} = V_{L2} = V_L$). All the different states described in Table 1 can be summarized as three kinds of working conditions: nonshoot-through, UST, and DST. They are shown in Figures 2(a)–2(c), respectively. From Figure 2(a), several equations can be derived as follows:

$$\begin{cases} V_C = 2V_{dc} - V_L, \\ V_i = V_C - V_L, \\ V_P = \dfrac{V_i}{2}, \\ V_O = 0, \\ V_N = -\dfrac{V_i}{2}. \end{cases} \tag{1}$$

Similarly, the equations derived from Figures 2(b) and 2(c) are as follows:

$$\begin{cases} V_L = V_{dc}, \\ V_i = V_C - V_L, \\ V_P = V_O = 0, \\ V_N = -V_i. \end{cases} \tag{2}$$

$$\begin{cases} V_L = V_{dc}, \\ V_i = V_C - V_L, \\ V_P = V_i, \\ V_N = V_O = 0. \end{cases} \tag{3}$$

Here, the time duration of UST status is denoted as T_{sh_U} and T_{sh_D} for DST status. Normally, T_{sh_U} should be equal to T_{sh_D} in order to reduce the output voltage harmonic components, which means

$$T_{sh\_U} = T_{sh\_U} = T_{sh}. \tag{4}$$

At the steady state, the average voltages across L_1 and L_2 keep zero over the sampling period T_S, and the following equation could be derived from equations (1)–(3):

$$2V_{dc} \cdot T_{sh} + (2V_{dc} - V_c) \cdot (T_S - 2T_{sh}) = 0. \tag{5}$$

$$\begin{aligned} V_C &= \frac{T_S - T_{sh}}{T_S - 2T_{sh}} \cdot 2V_{dc} = \frac{(1 - T_{sh}/T_S)}{(1 - 2T_{sh}/T_S)} \cdot 2V_{dc} \\ &= \frac{1 - D}{1 - 2D} \cdot 2V_{dc}, \end{aligned} \tag{6}$$

where $D = (T_{sh}/T_S)$ is defined as the duty ratio of the shoot-through states.

According to equations (1) and (6), for the nonshoot-through state, the output voltage V_i could be obtained as

$$\begin{aligned} V_i &= V_C - V_L = 2(V_C - V_{dc}), \\ &= 2\left(\frac{1 - D}{1 - 2D} 2V_{dc} - V_{dc}\right) = \frac{1}{1 - 2D} 2V_{dc}. \end{aligned} \tag{7}$$

For the Up or Down shoot-through states, the output voltage V_i could be obtained according to equations (2), (3), and (6):

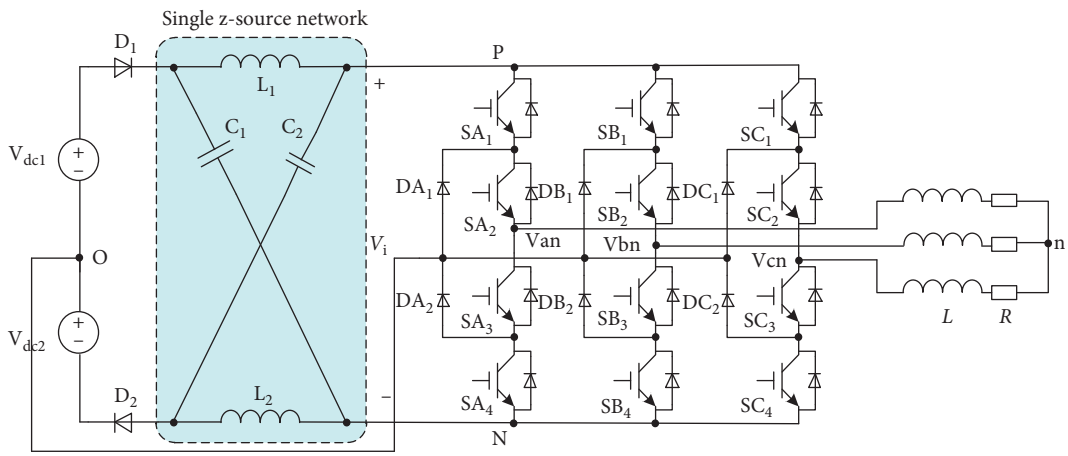

Figure 1: Topology of the NPC three-level ZSC.

Table 1: Different states and output voltage.

Mode	Turn-on switches	Output voltage
1	SX_1, SX_2, D_1, D_2	$V_i/2$
0	SX_2, SX_3, D_1, D_2	0
−1	SX_3, SX_4, D_1, D_2	$-V_i/2$
U	SX_1, SX_2, SX_3, D_1	0 or $-V_i$
D	SX_2, SX_3, SX_4, D_2	0 or V_i

Here, $X = A$, B, or C.

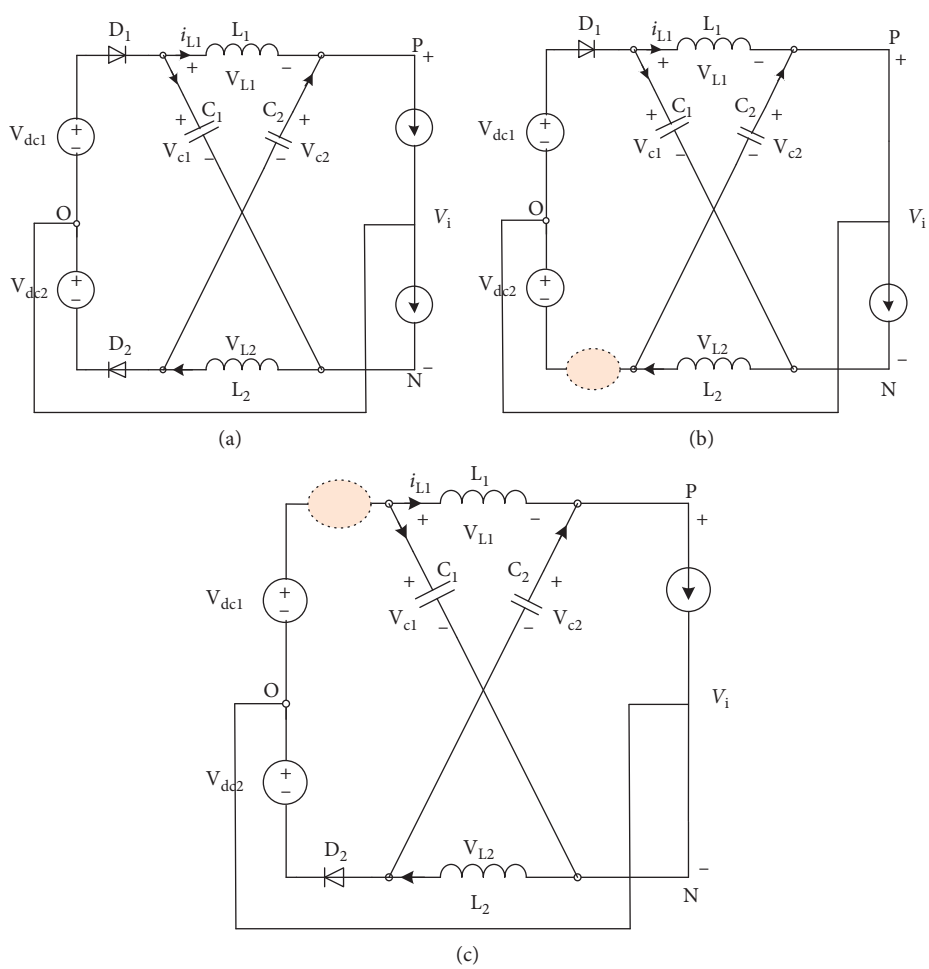

Figure 2: Equivalent circuits of the different states. (a) Nonshoot-through (b) Up shoot-through. (c) Down shoot-through.

$$V_{\mathrm{i}} = V_{\mathrm{C}} - V_{\mathrm{L}} = V_{\mathrm{C}} - V_{\mathrm{dc}},$$
$$= \frac{1-D}{1-2D} 2V_{\mathrm{dc}} - V_{\mathrm{dc}} = \frac{1}{1-2D} V_{\mathrm{dc}}. \tag{8}$$

Now, the three output voltages could also be represented as

$$V_{\mathrm{P}} = \frac{V_{\mathrm{dc}}}{1-2D},$$
$$V_{\mathrm{O}} = 0, \tag{9}$$
$$V_{\mathrm{N}} = -\frac{V_{\mathrm{dc}}}{1-2D}.$$

And the output phase voltage U_x could be derived as

$$U_x = M \cdot \frac{V_{\mathrm{dc}}}{1-2D} = MH \cdot V_{\mathrm{dc}}, \quad x = a, b, c, \tag{10}$$

where M is the modulation coefficient and $H = 1/(1\text{-}2D)$ represents the booster ratio.

3. An Improved MPC-Based SVPWM Mechanism

3.1. Traditional MPC. The mathematical model of the NPC three-level ZSC in $\alpha\beta$ coordinates can be given as

$$u_{\alpha,\beta} = L\frac{\mathrm{d}i_{\alpha,\beta}}{\mathrm{d}t} + Ri_{\alpha,\beta}, \tag{11}$$

where R and L are the load resistance and inductance, respectively.

By using the Euler approximation for a sampling time T_{s} (shown in equation (12)), equation (10) is discretized as in equation (13):

$$\frac{\mathrm{d}x(t)}{\mathrm{d}t} = \frac{x(k+1) - x(k)}{T_s}, \tag{12}$$

$$i_{\alpha,\beta}(k+1) = \left[1 - \frac{T_s R}{L}\right] i_{\alpha,\beta}(k) + \frac{T_s}{L} u_{\alpha,\beta}(k), \tag{13}$$

where $i_{\alpha,\beta}$ is the output current in $\alpha\beta$ coordinates, $u_{\alpha,\beta}$ stands for the output voltage also in $\alpha\beta$ coordinates, which is determined by the 27 switching states of the NPC three-level ZSC, and k is the kth sampling period.

From this mathematical model, the predictive output current at $(k+1)$th could be derived as

$$i^P_{\alpha,\beta}(k+1) = \left[1 - \frac{T_s R}{L}\right] i_{\alpha,\beta}(k) + \frac{T_s}{L} u_{\alpha,\beta}(k). \tag{14}$$

For the traditional MPC strategy, a roll optimization of objective function could be set, as shown in equation (15), for the current trajectory control:

$$g = \left|i^*_\alpha(k+1) - i^P_\alpha(k+1)\right| + \left|i^*_\beta(k+1) - i^P_\beta(k+1)\right|, \tag{15}$$

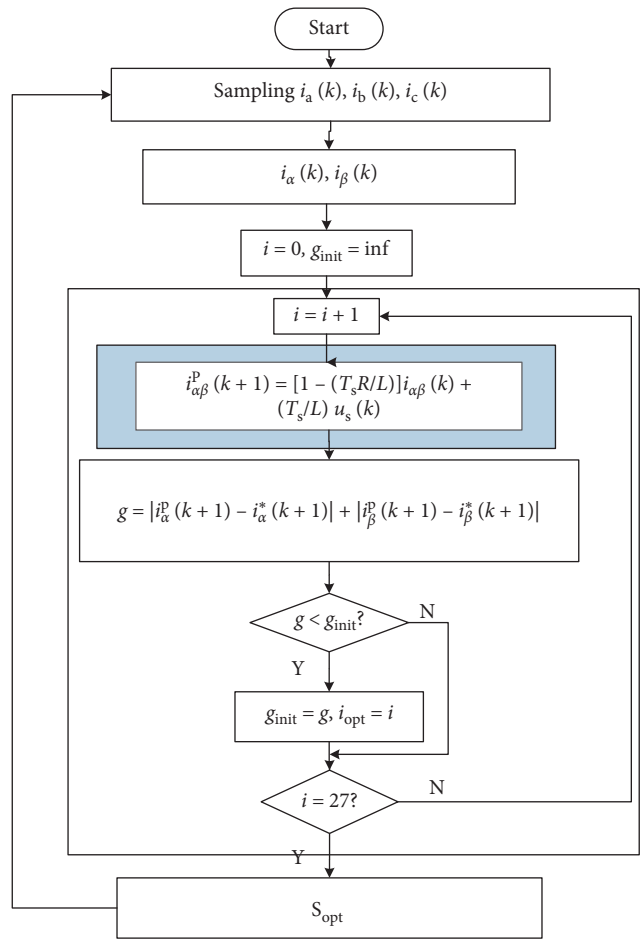

Figure 3: Implementation flow chart of the traditional MPC.

where $i^*_\alpha(k+1)$ and $i^*_\beta(k+1)$ are the given current components, respectively, and $i^{\mathrm{P}}_\alpha(k+1)$ and $i^{\mathrm{P}}_\beta(k+1)$ are the predictive current components from equation (14).

Obviously, for this traditional method, 27 cycles of optimization should be conducted to obtain the smallest g and the corresponding optimal switching state, in which equation (13) need to be also calculated 27 times in order to obtain the current components with different input voltages, which significantly increases the computation consumption. The implementation flow chart of the traditional MPC strategy is shown in Figure 3.

3.2. Improved MPC. For equation (14), the input voltage can be represented as

$$u_{\alpha,\beta}(k) = \frac{L}{T_s}\left[i^P_{\alpha,\beta}(k+1) - i_{\alpha,\beta}\right] + Ri_{\alpha,\beta}(k). \tag{16}$$

Assume that the predictive output current in equation (15) equals the given current components in ideal condition, which means

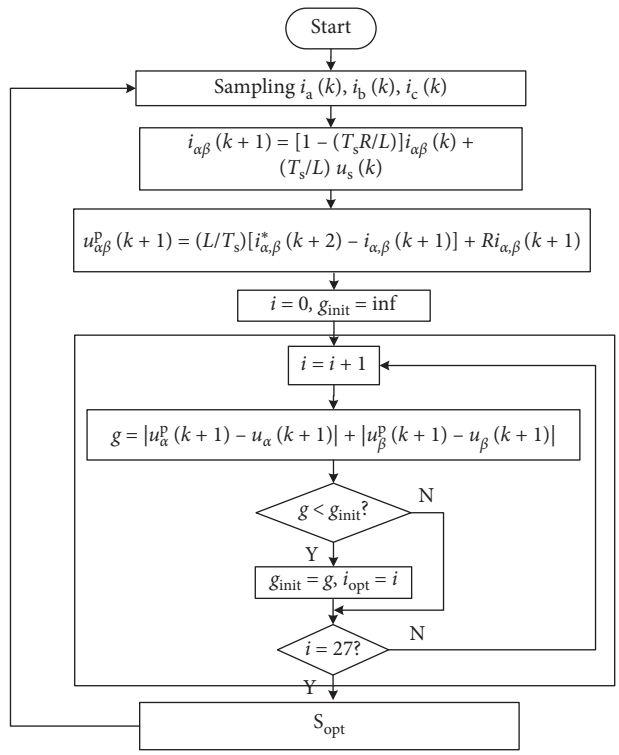

Figure 4: Implementation flow chart of the improved MPC.

$$i^*_{\alpha,\beta}(k+1) = i^p_{\alpha,\beta}(k+1). \tag{17}$$

With the combination of equations (16) and (17), the predictive voltage components $u^p_{\alpha,\beta}(k)$ could be obtained as

$$u^p_{\alpha,\beta}(k) = \frac{L}{T_s}\left(i^*_{\alpha,\beta}(k+1) - i_{\alpha,\beta}(k)\right) + Ri_{\alpha,\beta}(k), \tag{18}$$

where superscript "p" means the expected value and $i^*_{\alpha,\beta}(k+1)$ is the reference current at $(k+1)$th sampling, while the $i_{\alpha,\beta}(k)$ is the actual current at kth sampling.

For the improved MPC strategy, the roll optimization of objective function was set as

$$g = \left|u^p_\alpha(k) - u_\alpha(k)\right| + \left|u^p_\beta(k) - u_\beta(k)\right|. \tag{19}$$

In order to make compensation of the time delay, equations (18) and (19) are shifted one step forward. Thus, the predictive voltage components and the objective function at $(k+1)$th could be derived as equations (20) and (21):

$$u^p_{\alpha,\beta}(k+1) = \frac{L}{T_s}\left(i^*_{\alpha,\beta}(k+2) - i_{\alpha,\beta}(k+1)\right) + Ri_{\alpha,\beta}(k+1), \tag{20}$$

$$g = \left|u^p_\alpha(k+1) - u_\alpha(k+1)\right| + \left|u^p_\beta(k+1) - u_\beta(k+1)\right|. \tag{21}$$

The implementation flow chart of this improved MPC strategy then could be derived, as shown in Figure 4.

It is obvious that, for the improved MPC, the current calculation within the roll optimization has been omitted, which could improve the execution efficiency to a great degree.

On the other aspect, for the prediction accuracy, the predictive voltage error could be derived with equations (16) and (18):

$$\begin{aligned}\left|u^p_{\alpha\beta}(k) - u_{\alpha\beta}(k)\right| &= \left|\left\{\frac{L}{T_s}\left(i^*_{\alpha,\beta}(k+1) - i_{\alpha,\beta}(k)\right) + Ri_{\alpha,\beta}(k)\right\}\right. \\ &\quad \left. - \left\{\frac{L}{T_s}\left(i^p_{\alpha,\beta}(k+1) - i_{\alpha,\beta}(k)\right) + Ri_{\alpha,\beta}(k)\right\}\right|, \\ &= \frac{L}{T_s}\left|i^*_{\alpha,\beta}(k+1) - i^p_{\alpha,\beta}(k+1)\right|.\end{aligned} \tag{22}$$

From (22), it can be seen that the voltage tracking performance is consistent with the current, which provides the validation of the proposed improved MPC strategy.

3.3. Insertion of the Shoot-Through States. For both the traditional and improved MPC strategies, their output frequency is a varying variable, which is unsuitable for the filtering design. Here, the optimized voltage $u_{opt}(k)$ (the corresponding switch state is S_{opt}) has been implemented by the basic space voltage vectors and based on which the shoot-through states of the Z-source are inserted to ensure the boost performance. The MPC-based SVPWM mechanism is shown in Figure 5.

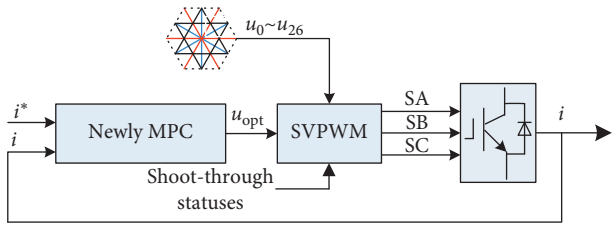

Figure 5: MPC-based SVPWM mechanism.

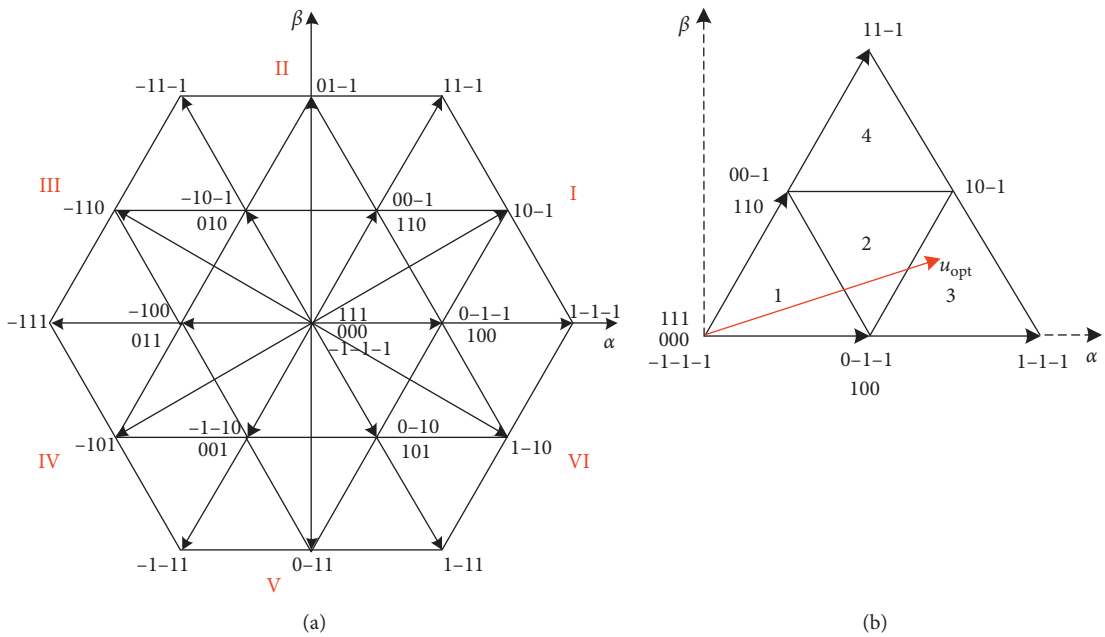

Figure 6: Space voltage vectors of the NPC three-level converter. (a) Space voltage vectors. (b) Space voltage vectors in Zone I.

Shoot-trough states' insertion not only determines the boost performance but also affects the output harmonic distortion and the switch losses. For the space voltage vectors shown in Figure 6(a), it is being taken as an example that the obtained optimized voltage u_{opt} locates in Zone I and triangle 3, as shown in Figure 6(b).

Assume that the initial switch state is "0 −1 −1," which means SA2, SA3, SB3, SB4, SC3, and SC4 are turned ON:

(1) At $t = t1$, state "0 −1 −1" should be switched to "1 −1 −1" (for phase A, SA is changed from "0" to "1"), and the UST could be inserted in phase A by previously turning on the switch "SA1," as shown in Figure 7 (SA1, SA2, and SA3 are ON while SA4 are OFF). During this insertion, the switch states for phases B and C remain unchanged, which satisfy the "volt-second" principle.

(2) At $t = t2$, state "1 −1 −1" should be switched to "1 0 −1" (for phase B, SB is changed from "−1" to "0"). If the UST is previously inserted in phase B, the switch state of phase A could be kept as "1," while the switch state of phase C should be clamped from "−1" to "0," which means the "volt-second" state would be destroyed so this insertion should be omitted.

(3) At $t = t3$, state "1 0−1" should be switched to "1 0 0" (for phase C, SC is changed from "−1" to "0"). The DST could be inserted in phase C by persistently turning on the switch "SC4," as shown in Figure 7 (SC2, SC3, and SC4 are ON while SC1 are OFF). During this insertion, the switch states for phases A and B remain unchanged, which satisfy the "volt-second" principle.

Obviously, when the reference vector is located in Zone I and triangle 3, the UST and DST can be inserted in the interaction range of the equivalent zero vector. Thus, the condition of $T_{sh\_U} = T_{sh\_D}$ can ensure the balance of the UST status and the DST status.

From Figure 7, it could be easily seen that both the up and down shoot-through states would increase the output voltage (comparing Ref.Va(SA') and Ref.Va(SA) and Ref.Vc(SC') and Ref.Vc(SC)).

4. Experimental Results

In this paper, the effectiveness of the proposed improved MPC-based SVPWM mechanism is verified via an

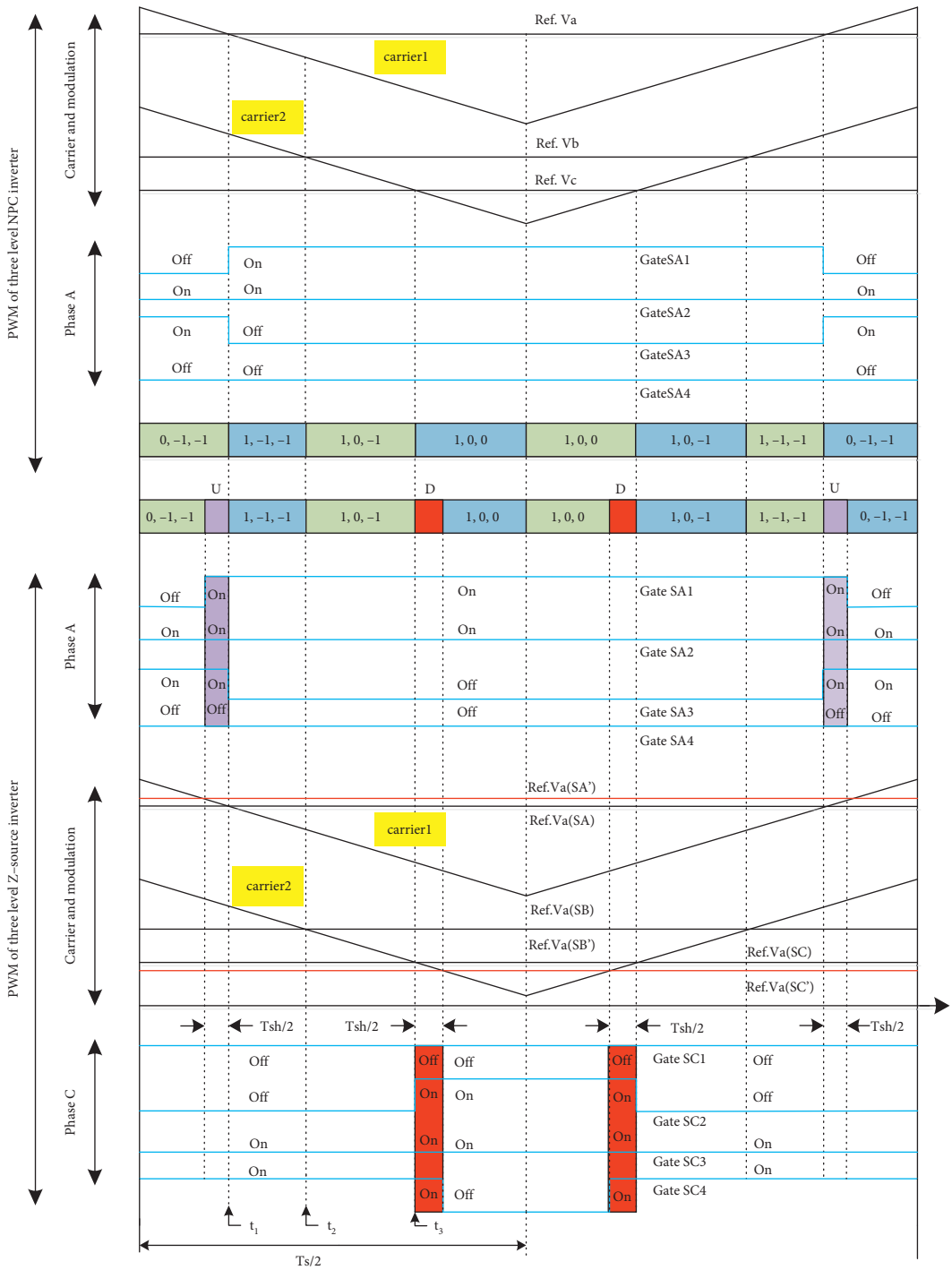

Figure 7: Insertion strategy (Zone I and triangle 3).

established experimental platform, as shown in Figure 8, along with the deep comparisons with the traditional SVPWM method. The detailed parameters are listed in Table 2. The control algorithm is implemented on a TMS320F28335 DSP with floating-point arithmetic.

Firstly, when the input voltage V_{dc} changes from 100 V to 200 V ($V_{dc1} = V_{dc2}$ change from 50 V to 100 V), the corresponding dynamical line and phase voltages of the improved strategy are shown in Figure 9.

However, because of the voltage prediction error shown in Figure 10, there is some voltage ripple existing in the DC-link voltage.

When the duty ratio D changes from 0 to 0.3, which means the output voltage of the Z-source topology V_i could be 2.5 times as much as the input voltage V_{dc} (according to equation (7)), the dynamical output line and phase voltages u_{ab} and u_a from the traditional SVPWM method and the improved proposed MPC-based

Figure 8: Experimental platform.

Table 2: Platform parameters.

Parameters	Value
DC-link voltage ($V_{dc1} = V_{dc2}$) (V)	50
Inductance of Z-source ($L_1 = L_2$) (mH)	2
Capacitance of Z-source ($C_1 = C_2$) (μF)	100
Load inductance (mH)	5
Load resistance (Ω)	10
Sampling frequency (Hz)	10 k
Reference current's amplitude (A)	10
Duty ratio(D)	0->0.3

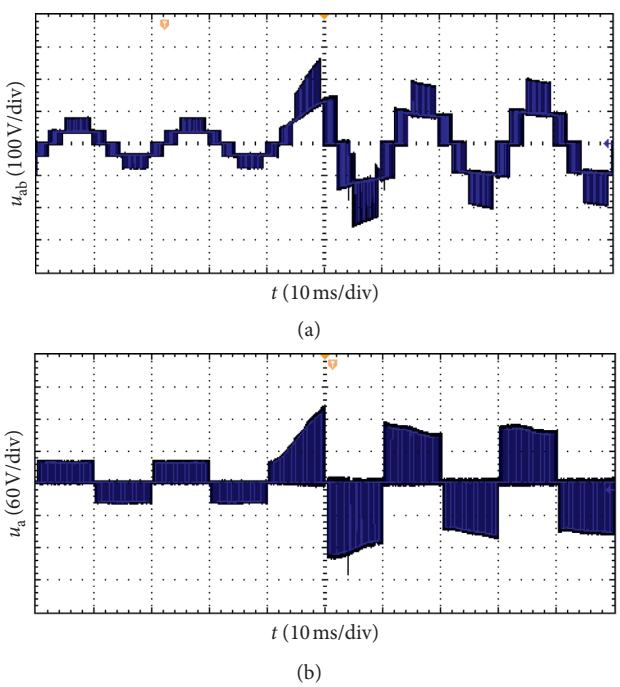

Figure 9: Dynamical line and phase voltages of the improved MPC-based SVPWM mechanism. (a) Line voltage u_{ab}. (b) Phase voltage u_a.

SVPWM mechanism are shown in Figures 11 and 12, respectively.

Correspondingly, the output voltage V_i and the capacitors' voltages V_{c1} and V_{c2} are shown in Figures 13 and 14. It is obvious that V_i changes from 100 V to about 250 V and the

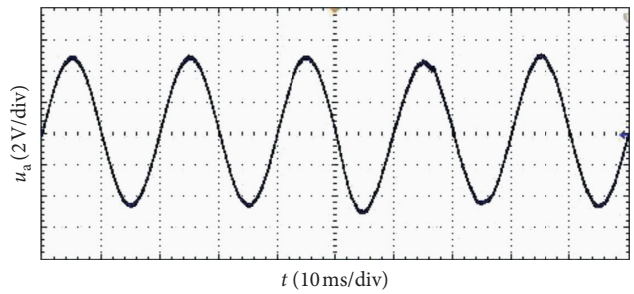

Figure 10: Voltage prediction error.

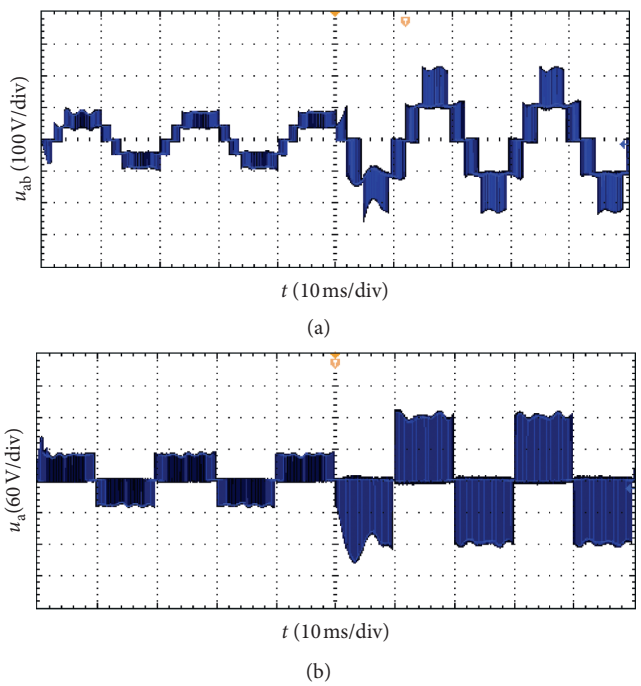

Figure 11: (a) Line voltage u_{ab} and (b) Phase voltage u_a of the traditional SVPWM.

capacitors' voltages are basically guaranteed to be in equilibrium.

For the output current, the dynamic comparisons are shown in Figures 15 and 16 along with the harmonic distortion analysis by taking a-phase current as an example.

From Figures 15 and 16, it can be seen that the harmonic distortion changes from 3.69% to 2.11% for the traditional and improved methods without the booster function ($D = 0$), while from 4.20% to 3.53% with the insertion of the shoot-through states ($D = 0.3$), which could make verification of the improved mechanism studied in this paper. Besides, with the improved MPC-based SVPWM mechanism, the harmonic frequency is a relative fixed value, which is suitable for the filter designing. Besides, after the dynamic change, the restability time is about half an cycle for this improved MPC-based SVPWM, which is faster than the traditional SVPWM method (about one cycle).

In order to exhibit the superior property of the improved MPC-based SVPWM mechanism. The execution

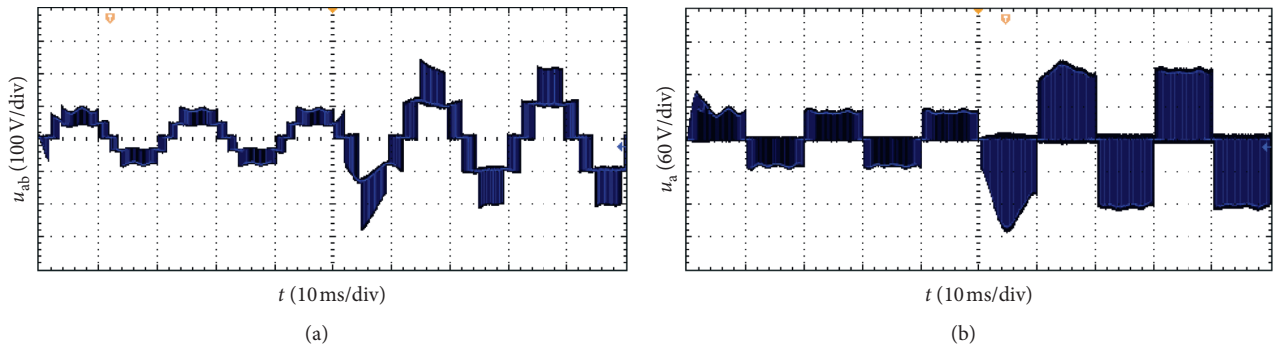

Figure 12: (a) Line voltage u_{ab}. (b) Phase voltage u_a of the improved strategy.

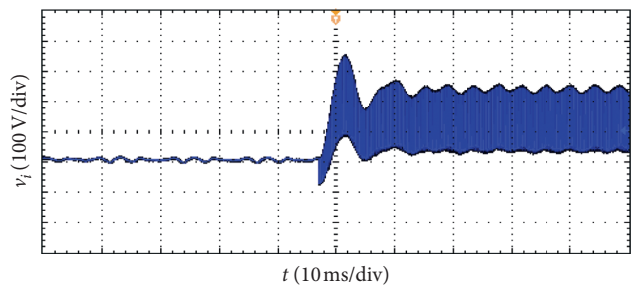

Figure 13: Output voltage V_i.

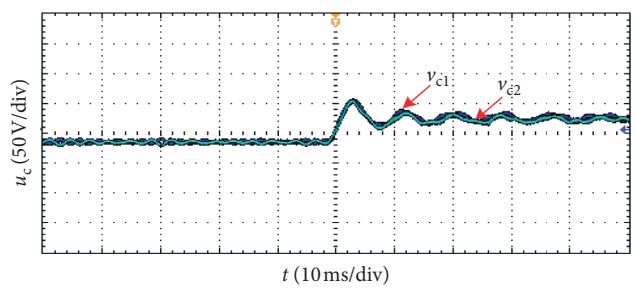

Figure 14: Capacitors' voltages V_{C1} and V_{C2}.

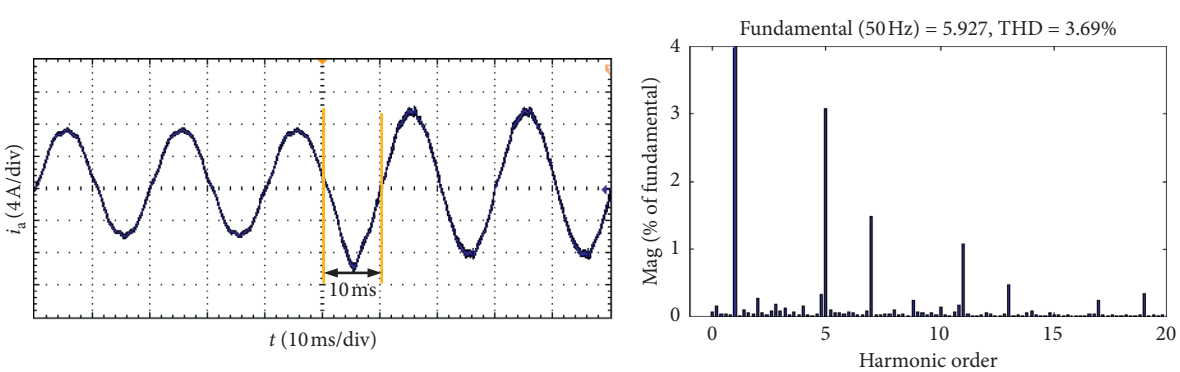

Figure 15: Continued.

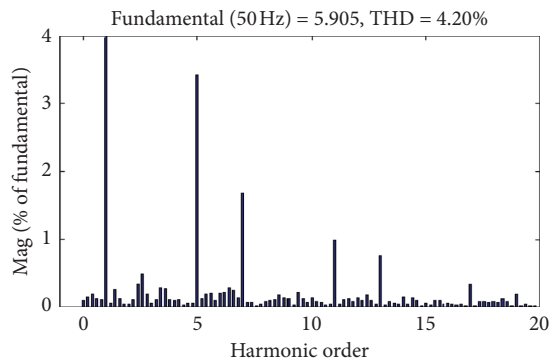

(c)

Figure 15: Dynamic current waveform and the corresponding THD analysis of the traditional SVPWM method. (a) Dynamic a-phase current i_a. (b) THD of i_a when $D = 0$. (c) THD of i_a when $D = 0.3$.

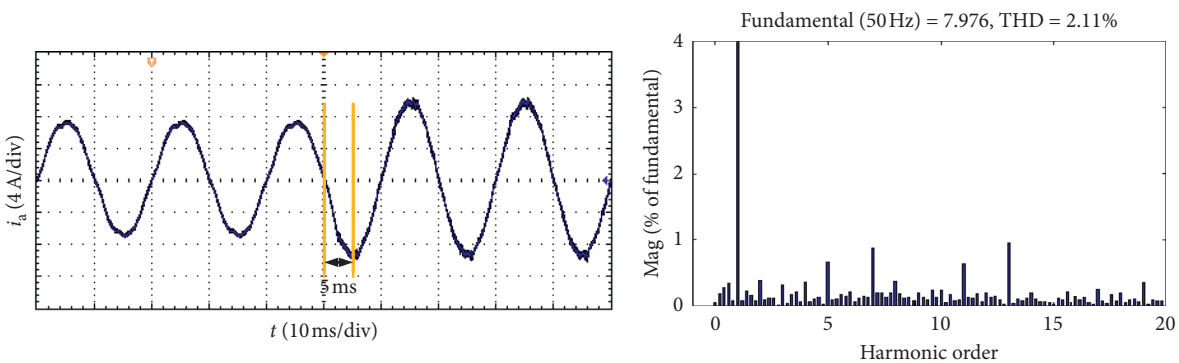

(a) (b)

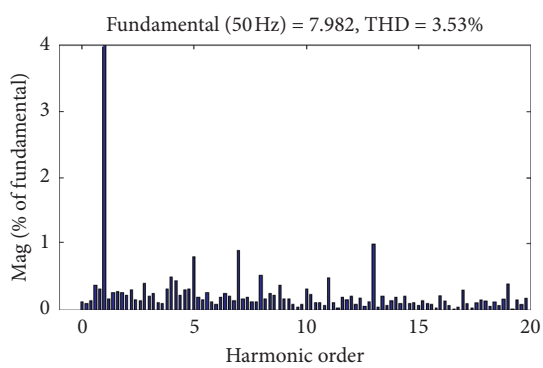

(c)

Figure 16: Dynamic current waveform and the corresponding THD analysis of the improved MPC-based SVPWM mechanism. (a) Dynamic a-phase current i_a. (b) THD of i_a when (D) = 0. (c) THD of i_a when (D) = 0.3.

time comparisons between the proposed method, the traditional SVPWM, and the normal MPC-based SVPWM are summarized in Table 3, where the execution time is calculated by averaging ten-time measured results when $D = 0$ and $D = 0.3$ and the sampling frequency is 10 kHz.

For the normal MPC-based SVPWM method, it has 10.03% and 13.91% time savings than the traditional SVPWM for the complicated trigonometric calculations has been omitted. Similarly, for the calculation reduction in the roll optimization, the improved scheme has over 26.25% and 19.25% time saving improvements than the traditional SVPWM and the normal MPC-based SVPWM when $D = 0$, while 28.78% and 17.27% when $D = 0.3$.

Table 3: Execution time comparisons.

	Traditional SVPWM (μs)	Normal MPC-based SVPWM (μs)	Improved MPC-based SVPWM (μs)
$D = 0$	18.13	16.31	13.37
$D = 0.3$	19.91	17.14	14.18

5. Conclusions

In this paper an improved MPC-based SVPWM mechanism has been proposed for the NPC three-level ZSC. Firstly, in order to improve the execution efficiency, a novel voltage prediction has been derived based on the mathematical models to replace the normal current prediction, by which the optimization could be effectively simplified along with a relative nice performance. Besides, with the combination of the improved MPC and SVPWM, the harmonic frequency of the output current could be kept relatively fixed to be suitable for the filtering design and the shoot-through states insertions have been also studied to realize the voltage boosting. Lastly, comparison experiments have been carried out to make verification of this improved MPC-based SVPWM mechanism. In particular, this improved method has a similar static performance to the traditional SVPWM with a better dynamic performance, while for the execution efficiency, it has over 26.25% and 19.25% time saving improvements than the traditional SVPWM and the normal MPC-based SVPWM when $D = 0$, while 28.78% and 17.27% when $D = 0.3$, which is suitable for the digital implementation.

Data Availability

The processed data required to reproduce these findings cannot be shared at this time as the data also forms part of an ongoing study.

Conflicts of Interest

The authors declare that they have no conflicts of interest.

Acknowledgments

This work was supported by Research Foundation of JiangSu Collaborative Innovation Center for Building Energy Saving and Construction Technology (no. SJXTBS1704); Jiangsu University Natural Science Research Project (No. 18KJB470024).

References

[1] Q. Yuan, J. Qian, H. Wu, W. Yin, and Q. Jiang, "Stator current harmonic elimination control for the high-power synchronous motors with online implementation," *IET Power Electronics*, vol. 12, no. 4, pp. 801–809, 2019.

[2] R. Vargas, P. Cortés, U. Ammann, J. Rodriguez, and J. Pontt, "Predictive control of a three-phase neutral-point-clamped inverter," *IEEE Transactions on Industrial Electronics*, vol. 54, no. 5, pp. 2697–2705, 2007.

[3] Z. Fang, "Z-source inverter," *IEEE Transactions On Industry Applications*, vol. 39, no. 2, pp. 504–510, 2003.

[4] Y. Zhang, C. Fu, M. Sumner, and P. Wang, "A wide input-voltage range quasi-Z-source boost DC-DC converter with high-voltage gain for fuel cell vehicles," *IEEE Transactions on Industrial Electronics*, vol. 65, no. 6, pp. 5201–5212, 2018.

[5] F. Z. Peng, M. Shen, and K. Holland, "Application of Z-source inverter for traction drive of fuel cell-battery hybrid electric vehicles," *IEEE Transactions on Power Electronics*, vol. 22, no. 3, pp. 1054–1061, 2007.

[6] P. C. Loh, F. Gao, F. Blaabjerg, and S. W. Lim, "Operational analysis and modulation control of three-level Z-source inverters with enhanced output waveform quality," *IEEE Transactions on Power Electronics*, vol. 24, no. 7, pp. 1767–1775, 2009.

[7] X. Guo, Y. Yang, and T. Zhu, "ESI: a novel three-phase inverter with leakage current attenuation for transformerless PV systems," *IEEE Transactions on Industrial Electronics*, vol. 65, no. 4, pp. 2967–2974, 2018.

[8] F. Gao, P. C. Loh, F. Blaabjerg, and D. M. Vilathgamuwa, "Performance evaluation of three-level Z-source inverters under semiconductor-failure conditions," *IEEE Transactions on Industry Applications*, vol. 45, no. 3, pp. 971–981, May. 2009.

[9] J. Liu, J. Wu, J. Qiu, and J. Zeng, "Switched Z-source/quasi-Z-source DC-DC converters with reduced passive components for photovoltaic systems," *IEEE Access*, vol. 7, pp. 40893–40903, 2019.

[10] X. Zeng, Y. Yang, B. Wang, and F. Blaabjerg, "Leakage current reduction of three-phase Z-source three-level four-leg inverter for transformerless PV system," *IEEE Transactions on Power Electronics*, vol. 34, no. 7, pp. 6299–6308, 2019.

[11] A. Blaabjerg, E.-H. Miliani, S. Pierfederici, and F. Meibody-Tabar, "A novel quasi-Z-source inverter topology with special coupled inductors for input current ripples cancellation," *IEEE Transactions on Power Electronics*, vol. 31, no. 3, pp. 2409–2416, Mar. 2016.

[12] X. Guo, Y. Yang, R. He, B. Wang, and F. Blaabjerg, "Transformerless Z-source four-leg PV inverter with leakage current reduction," *IEEE Transactions on Power Electronics*, vol. 34, no. 5, pp. 4343–4352, May. 2019.

[13] M. Wang, J. S. Moghani, and J. Milimonfared, "A novel dual switching frequency modulation for Z-source and quasi-Z-source inverters," *IEEE Transactions on Industrial Electronics*, vol. 65, no. 6, pp. 5167–5176, 2018.

[14] A. Abdelhakim, P. Davari, F. Blaabjerg, and P. Mattavelli, "Switching loss reduction in the three-phase quasi-Z-source inverters utilizing modified space vector modulation strategies," *IEEE Transactions on Power Electronics*, vol. 33, no. 5, pp. 4045–4060, 2018.

[15] X. Mattavelli, J. Zou, J. Zhao et al., "A novel model predictive control strategy to eliminate zero-sequence circulating current in paralleled three-level inverters," *IEEE Journal of Emerging and Selected Topics in Power Electronics*, vol. 7, no. 1, pp. 309–320, Mar. 2019.

[16] B. Hu, L. Kang, J. Liu, J. Zeng, S. Wang, and Z. Zhang, "Model predictive direct power control with fixed switching frequency and computational amount reduction," *IEEE Journal of Emerging and Selected Topics in Power Electronics*, vol. 7, no. 2, pp. 956–966, Jun. 2019.

[17] M. Mosa, R. S. Balog, and H. Abu-Rub, "High-performance predictive control of quasi-impedance source inverter," *IEEE Transactions on Power Electronics*, vol. 32, no. 4, pp. 3251–3262, 2017.

[18] S. Bayhan, M. Trabelsi, H. Abu-Rub, and M. Malinowski, "Finite-control-set model-predictive control for a quasi-Z-source four-leg inverter under unbalanced load condition," *IEEE Transactions on Industrial Electronics*, vol. 64, no. 4, pp. 2560–2569, Apr. 2017.

[19] A. Ayad, P. Karamanakos, and R. Kennel, "Direct model predictive current control strategy of quasi-Z-source

inverters," *IEEE Transactions on Power Electronics*, vol. 32, no. 7, pp. 5786–5801, 2017.

[20] Y. Liu, H. Abu-Rub, Y. Xue, and F. Tao, "A discrete-time average model-based predictive control for a quasi-Z-source inverter," *IEEE Transactions on Industrial Electronics*, vol. 65, no. 8, pp. 6044–6054, 2018.

[21] L. He, J. Nai, and J. Zhang, "Single-phase safe-commutation trans-Z-source AC-AC converter with continuous input current," *IEEE Transactions on Industrial Electronics*, vol. 65, no. 6, pp. 5135–5145, 2018.

[22] V.-Q.-B. Ngo, M.-K. Nguyen, and T.-T. Tran, "A modified model predictive power control for grid-connected T-Type inverter with reduced computational complexity," *Electronics*, vol. 8, no. 2, 2019.